Article

Design and Stability Analysis of an Offshore Floating Multi-Wind Turbine Platform †

Srikanth Bashetty * and Selahattin Ozcelik

Frank H. Dotterweich College of Engineering, Texas A&M University, Kingsville, TX 78363, USA; selahattin.ozcelik@tamuk.edu
* Correspondence: srikanth.bashetty@tamuk.edu
† This paper is an extended version of our paper published in 2020 IEEE Green Technologies Conference (GreenTech), Oklahoma City, OK, USA, 1–3 April 2020; pp. 184–189.

Abstract: The multi-wind turbine platform technology has the potential to harness the significant source of offshore wind energy in deep waters. However, the wake interference between the turbines on the multi-wind turbine platform can cause a reduction in power production; hence, it is important to study the wake effects in the initial phase of the design. This paper studies the effects of wake interference between the wind turbines on three different platform configurations to find a suitable configuration for the wind turbines on a multi-turbine platform. The analytical Larsen wake model and computational fluid dynamics (CFD) simulations are used for evaluating the wake effects. The platform configuration required for the wind turbines is determined based on the results of wake effects, and then a novel platform is designed. The free-floating stability behavior of the multi-wind turbine platform is analyzed using the hydrostatic analysis of the modeled platform. The wave-body interaction between the platform and the waves is predicted using the hydrodynamic analysis. A preliminary cost analysis of the multi-turbine platform concept is evaluated and compared with a single wind turbine floating concept. The results showed that the presented design is a promising concept that can enhance the offshore wind industry.

Keywords: offshore floating platform; wake loss models; computational fluid dynamics; stability analysis; hydrodynamics

1. Introduction

Wind power has become one of the leading sources of renewable energy generation around the globe and a major source of electricity supply in the United States since the beginning of the 21st century [1]. The wind resources are abundant offshore, more specifically in deep waters at depths greater than 50 m in the regions near highly populated coastal states. For harnessing these deep-water wind resources, the wind turbines need floating platforms. The four important floating platform concepts are buoyancy- and ballast-stabilized semi-submersible [2–5], buoyancy-stabilized barge [6], ballast-stabilized spar buoy [7–9], and mooring line-stabilized tension leg platform [10–12]. The type of floating platform is selected based on the mooring system, the number of wind turbines, site requirements, construction, grid connection, and operating conditions of the sea [13]. Recently, the concept of multiple wind turbines on a floating platform has drawn attention because they are more stable and enable the use of higher towers and hence greater capture of wind energy [14–23]. The installation and mooring costs can be reduced by employing multiple wind turbines on a single platform as they can share common mooring lines [24]. However, the wake interference between the wind turbines is the most challenging issue that needs to be addressed in the design phase of the system [25]. The wake effect is a phenomenon where the wind speed downstream of a turbine has reduced speed and increased turbulence, causing a 20% to 45% reduction in energy generation and increasing the mechanical loading on the downstream wind turbines [26,27]. The main idea of

this research is to model a floating platform that can arrange multiple wind turbines to minimize the wake effects on the downstream wind turbines and maximize aerodynamic performance. A semi-submersible platform is used because it can be fabricated at the dock and towed to its installation site, thereby reducing installation costs by eliminating the need for expensive marine cranes and construction barges [4].

Lefranc and Torud [14] conducted feasibility, design, and cost analysis for a semi-submersible platform with three wind turbines installed and showed that the wake interaction between upwind and downwind turbines was the most challenging issue and proved that the power loss due to the wake effect was significant at low velocities and almost unchanged at high velocities. They also proved that the economics of the multi-wind turbine concept were comparable to the current single platforms in terms of the cost of energy production. Hu et al. [15] experimented without considering wind on a 1:50 scale model of a semi-submersible floating multi-wind turbine platform to check the accuracy of the numerical models in predicting the wave-body interaction between the waves and the platform. The linear wave-body interactions were analyzed using the potential flow method and pressure distributions on the platform due to waves were calculated using the CFD model. A large semi-submersible platform with four wind turbines installed at each corner was designed by Kim et al. The hydrodynamic forces data were obtained using ANSYS AQWA and implemented in GL-DNV Bladed [28]. A square semi-submersible-type multi-unit floating offshore wind turbine (MUFOWT) platform was designed in South Korea that accommodates 3 MW wind turbines at the four corners. Six energy converters along with twenty-four-point power absorber-type linear generator-based wave energy converters (WEC) were also placed on platform sides. A series of model tests were performed on the scaled model of MUFOWT by the research institute in Korea. The dynamic motions of wave energy converters were excluded from the model tests by fixing them to the platform [16–18]. A similar type of hybrid wind-wave floating offshore platform was considered by Lee et al. [19] to analyze the multi-body hydrodynamic interactions in a frequency domain. Jang et al. [20] showed that the heave plates with a minimal increase of mass can reduce the pitch and heave motions of a multi-unit offshore floating wind turbine. The concept of a triangular-shaped floating platform with three wind turbines at each corner was presented in [21,22] that considered only hydrodynamic loads to study the motion and elastic responses of the structure. This concept used a wind-tracing floating structure with a single-point mooring system that allows for the entire platform to rotate in response to the change of the wind direction. Bae et al. [25] conducted a fully coupled dynamic analysis between the blades, towers, floater, drivetrains, and mooring framework of a multi-unit floating offshore wind turbine. However, the wake effects of the wind turbines were not considered in this study.

In this paper, the wake interference effects between the wind turbines are analyzed using an analytical Larsen wake loss model and the CFD method to find the wake expansion and velocity deficits downstream of the wind turbines. Initially, the wake effects on three different configurations have been investigated to select a suitable configuration. The velocity distribution calculated at the downstream turbine using the Larsen wake model is compared with the CFD simulations. The design aspects of the offshore floating multi-wind turbine platform for installing the five 8 MW wind turbines considering the main dimensions of the floater are presented. For the selected design case, the hydrostatic analysis is carried out to predict the floating stability. The hydrodynamic performance of the platform is evaluated to find the added mass, response amplitude operators (RAOs), pressures, and motions. The cost analysis of the proposed concept is presented and compared with a single wind turbine floating platform. This paper is an extended and more elaborated version of the work published in [29].

The rest of the paper is organized as follows. The materials and methods are provided in Section 2. The results of wake effect analysis, multi-wind turbine platform configuration, hydrostatic analysis, hydrodynamic analysis, and cost analysis of the configuration are discussed in Section 3. Section 4 discusses conclusions and suggestions for future work.

2. Materials and Methods

In this section, the Larsen wake loss model and RANS equations with the $k - \omega$ SST turbulence model are presented. The wake loss model and CFD method are used to calculate the downwind expansion of the wake and the wind speed distribution in the wake.

2.1. Larsen Wake Loss Model

The Larsen wake model is the analytical wake model that accurately predicts the wake behavior by including the turbulence intensity factor [13]. The analytical Larsen wake loss model [30–33] is based on the Prandtl turbulent boundary layer equations that afford the closed-form solutions for the wake diameter (D_w) and the mean wind speed (u_2) in the wake as a function of axial distance (x) and radial distance (r). The Larsen wake loss model is described as follows:

$$u_2 = \frac{8u_1}{9} \left[C_F A_{rotor}(x + x_0)^{-2} \right]^{\frac{1}{3}} \left[r^{\frac{3}{2}} \left(3c_1^2 C_F A_{rotor}(x + x_0) \right)^{-\frac{1}{2}} - \left(\frac{35}{2\pi} \right)^{\frac{3}{10}} \left(3c_1^2 \right)^{-\frac{1}{5}} \right]^2 \tag{1}$$

$$D_w = 2 \left(\frac{35}{2\pi} \right)^{\frac{1}{5}} \left(3c_1^2 \right)^{\frac{1}{5}} [C_F A_{rotor}(x + x_0)]^{\frac{1}{3}} \tag{2}$$

where u_1 is the mean wind speed and C_F is the thrust force coefficient of the upstream wind turbine, respectively, and A_{rotor} is the area of the rotor disk. The estimation of the thrust force coefficient is approximated as $7/u_1$ since the wind speed is between the cut-in and rated wind speed [34–36]. The estimation of parameters c_1 and x_0 is given by:

$$c_1 = \left[\frac{D_{eff}}{2} \right]^{\frac{5}{2}} \left(\frac{105}{2\pi} \right)^{-\frac{1}{2}} [C_F A_{rotor} x_0]^{-\frac{5}{6}} \tag{3}$$

$$x_0 = \frac{9.5 D_r}{\left(\frac{D_{9.5}}{D_{eff}} \right)^3 - 1} \tag{4}$$

where D_r is the rotor diameter and D_{eff} is the effective rotor diameter, given by:

$$D_{eff} = D_r \sqrt{\frac{1 + \sqrt{1 - C_F}}{2\sqrt{1 - C_F}}} \tag{5}$$

and $D_{9.5}$ is the wake diameter at a distance of 9.5 rotor diameters downstream of the turbine, given by:

$$D_{9.5} = [D_{nb} + \min(H, D_{nb})] \tag{6}$$

where H is the hub height of the upstream wind turbine and D_{nb} is given by:

$$D_{nb} = max[1.08 D_r, 1.08 D_r + 21.7 D_r (I_t - 0.05)] \tag{7}$$

where I_t is the total turbulence intensity, given as [37]:

$$I_t = \sqrt{I_a^2 + I_w^2} \tag{8}$$

where I_a is the atmospheric turbulence intensity assumed to be between 5% and 8% for offshore, which depends on the temperature variations between different altitudes [38–40], and I_w is the wake added turbulence for spacing larger than 2D as a function of axial distance (x) and is given by:

$$I_w = 0.29 \left(\frac{x}{D_r} \right)^{-\frac{1}{3}} \sqrt{1 - \sqrt{1 - C_F}} \tag{9}$$

2.2. CFD Model

The continuity equation and unsteady RANS equations with the $k - \omega$ shear stress transport turbulence model [41–43] are used for CFD calculations implemented in ANSYS Fluent. The equations can be expressed as follows:

$$\nabla.v = 0 \tag{10}$$

$$\frac{\partial \overline{v}}{\partial t} + (\overline{v}.\nabla)\overline{v} = -\frac{1}{\rho}\nabla\overline{p} + \nu\nabla^2\overline{v} - \nabla.\left(\overline{v' \, v'}\right) \tag{11}$$

$$\frac{\partial}{\partial t}(\rho k) + \nabla.(\rho k v) = \nabla.\left[\left(\mu + \frac{\mu_t}{\sigma_k}\right)\nabla k\right] + \widetilde{P}_k - \beta^*\rho k\omega \tag{12}$$

$$\frac{\partial}{\partial t}(\rho\omega) + \nabla.(\rho\omega v) = \nabla.\left[\left(\mu + \frac{\mu_t}{\sigma_{\omega,1}}\right)\nabla\omega\right] + \gamma_2 P_\omega - \beta_2\rho\omega^2 + 2\frac{\rho}{\sigma_{\omega,2}\omega}\frac{\partial k}{\partial x_k} \tag{13}$$

where v represents the velocity of the flow field, ρ is the density, p is the pressure, ν is the kinematic viscosity, and $\overline{v' \, v'}$ is the Reynolds stress tensor. k is the turbulent kinetic energy, ω is the specific dissipation rate, μ is the dynamic viscosity, and $\widetilde{P}_k$ and P_ω are the turbulence production terms. The model constants are defined in Table 1.

Table 1. Constants of the $k - \omega$ SST model.

σ_k	$\sigma_{\omega,1}$	$\sigma_{\omega,2}$	γ_2	β_2	β^*
1	2	1.17	0.44	0.083	0.09

3. Results and Discussion

3.1. Wake Effect Analysis

Larsen's wake loss model is implemented in MATLAB to calculate the wake diameter and the velocity deficit in the wake for three platform configurations. CFD calculations based on the continuity equation and the nonlinear Reynolds-averaged Navier–Stokes (RANS) equations, with a standard $k - \omega$ shear stress transport (SST) closure for turbulence, are performed in ANSYS Fluent to compare with the results of the analytical Larsen wake model [44].

For downstream wind turbines, there is a possibility of wake overlap, and if the overlap of the wake is from two upstream wind turbines, then the wind speed can be estimated as the average of the wind speeds [26,45]. The three platform configurations considered for this study are square, pentagon, and hexagon-shaped platforms. For a square-type platform configuration, the four wind turbines are placed at each corner, separated by a distance of 2.75 times the rotor diameter in the crosswind and downwind directions. For pentagon and hexagon platform configurations, the wind turbines are arranged in three rows. For the pentagon platform, the 2 wind turbines (T1 and T2) in the first row are 1.5 rotor diameters apart in crosswind direction, the third-row turbine (T5) is placed at a 2.75 D_r distance downstream of the first row, and the 2 turbines in the second row (T3 and T4) are placed in between the first and third row in the windward direction, whereas in the crosswind direction they are placed to avoid the wake expansion with an added 20% of the rotor diameter distance between the tip of the wake and the wind turbine rotor. The hexagon configuration is similar to the pentagon except for the two turbines (T5 and T6) in the third row instead of one. The Larsen wake loss model implemented on the three configurations using MATLAB is shown in Figures 1–3.
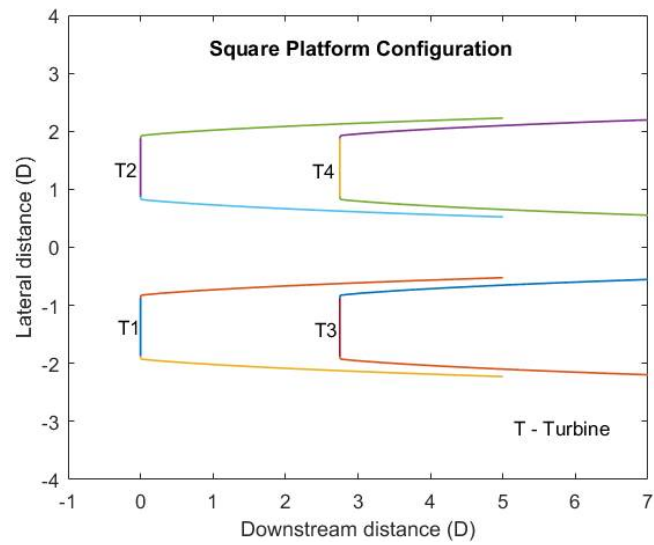
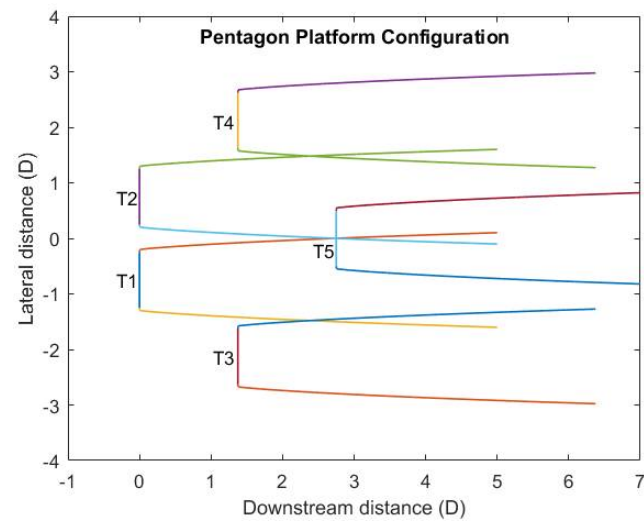**Figure 1.** Wake propagation for a square platform.

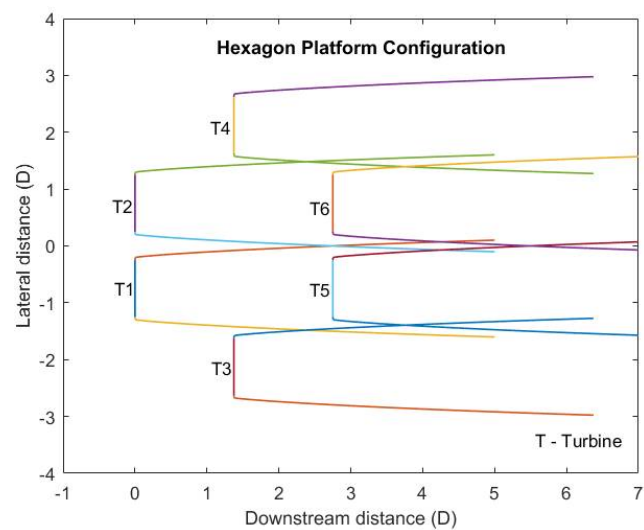**Figure 2.** Wake propagation for a pentagon platform.

Figure 3. Wake propagation for a hexagon platform.

The nonlinear wake expansion downstream of the wind turbines in the above figures shows that the rear wind turbines in the square platform (T3 and T4) and hexagon platform (T5 and T6) are in the direct wake of upstream turbines (T1 and T2), whereas in the pentagon platform, the rear wind turbine (T5) is in partial wake of the upstream turbines (T1 and T2). The value of u_1 considered for the wake analysis is 12.5 m/s, which is the rated wind speed of the reference wind turbine used for this study. The normalized average velocity profile along the downstream distance for a selected wind turbine is shown in Figure 4. It can be seen that there is a velocity deficit (u2 < u1) behind the rotor which can be correlated to the wind turbine wake that is surrounded by the varying turbulence intensity depicted in Figure 5. The turbulence intensity is related to the mean wind speed in the wake and the standard deviation (σ_u) in mean wind speed as $\frac{\sigma_u}{u_2}$ [46]. The streamwise velocity profiles near the downstream wind turbine at a 2.75 D_r distance downstream in the wake for the square (T3) and pentagon platform (T5) configurations are depicted in Figure 6. The velocity profile for the hexagon platform is not considered because it will be similar to the square platform as the downstream wind turbines in both cases are in the direct wake. The normalized average velocity along the radial distance for the square platform wind turbine is slightly lower relative to the pentagon platform near the center, which can correspond to the fact that the downstream wind turbine (T3 and T4) for the square platform is in direct wake, whereas for the pentagon platform (T5) it is in the partial wake. However, the normalized velocities in both cases become equal between 1 and 1.5 times the diameter distance.
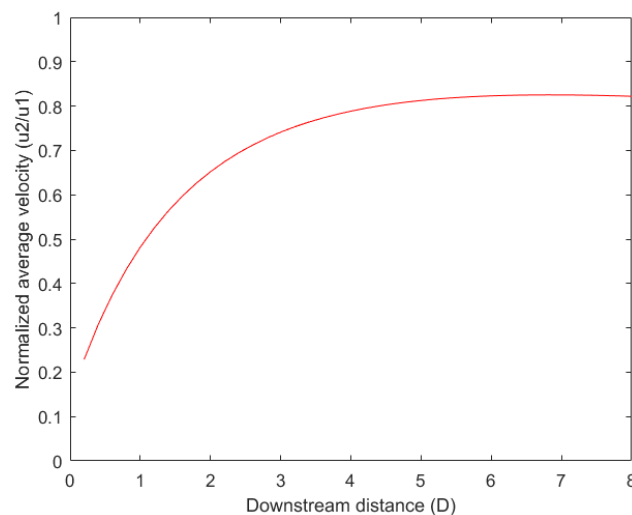

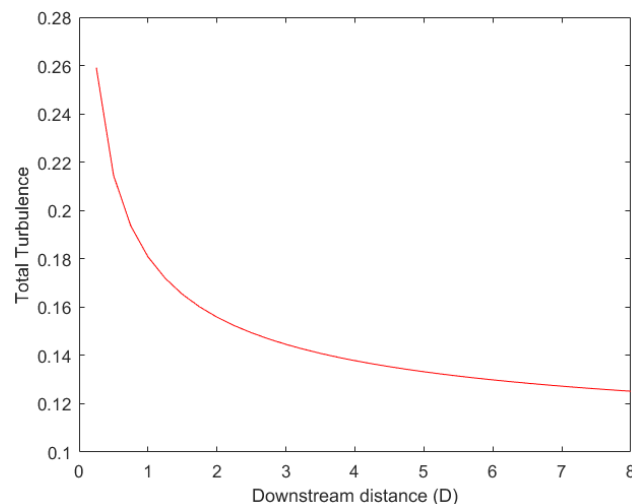**Figure 4.** Normalized average velocity profile for a selected wind turbine.

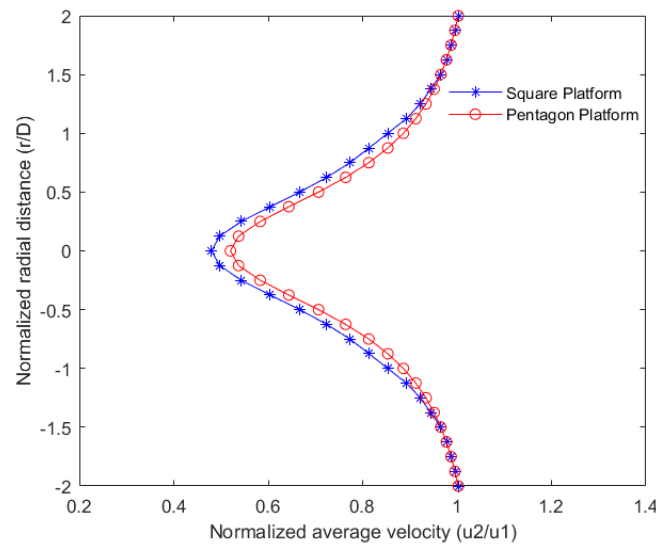**Figure 5.** Effective turbulence for a selected wind turbine.

Figure 6. Velocity profile of the downstream turbine.

In this study, the rotors of the configurations are modeled using an actuator disk technique [44]. The rectangular computational domain of dimensions 20D(X) × 15D(Y) is created in the ANSYS design modeler. The discretization of the model is performed using quadrilateral elements by employing refinement at the rotors. The wall boundary condition is imposed on the top and bottom boundaries of the computational domain. The three grid refinement levels used for generating the number of elements for the square configuration, pentagon configuration, and hexagon configuration are presented in Table 2. Different numbers of quadrangular layers and growth rates were used to develop the three meshes. An inflation tool with a growth rate of 1.2, 1.1, and 1.05 was used to obtain various levels of quadrangular cells in the boundary layer of the rotor disk so that y^+ is less than 1, as necessary by turbulence models [43,47,48]. To obtain the grid-independent results, different levels of grid refinements were tested in ANSYS Fluent to reach $y^+ < 1$ for all the conditions of the rotor. Figure 7 presents the mesh sensitivity study results in terms of a normalized velocity profile for turbine 5 of the pentagon platform configuration. This sensitivity study showed that mesh 2 and mesh 3 have approximately similar results and were found to have a satisfactory computational speed and accuracy, valid for all the simulated operating conditions.

Table 2. Mesh independence study characteristics.

| Type	Grid Features	Mesh 1	Mesh 2	Mesh 3
Square	Elements	1,021,500	2,122,370	3,982,860
	Global growth rate	1.2	1.1	1.05
	y^+ maximum	0.27	0.21	0.2
	Skewness maximum	0.8	0.73	0.72
Pentagon	Elements	1,050,600	2,150,730	4,050,340
	Global growth rate	1.2	1.1	1.05
	y^+ maximum	0.27	0.21	0.2
	Skewness maximum	0.8	0.73	0.72
Hexagon	Elements	1,065,000	2,163,740	4,122,610
	Global growth rate	1.2	1.1	1.05
	y^+ maximum	0.27	0.21	0.2
	Skewness maximum	0.8	0.73	0.72
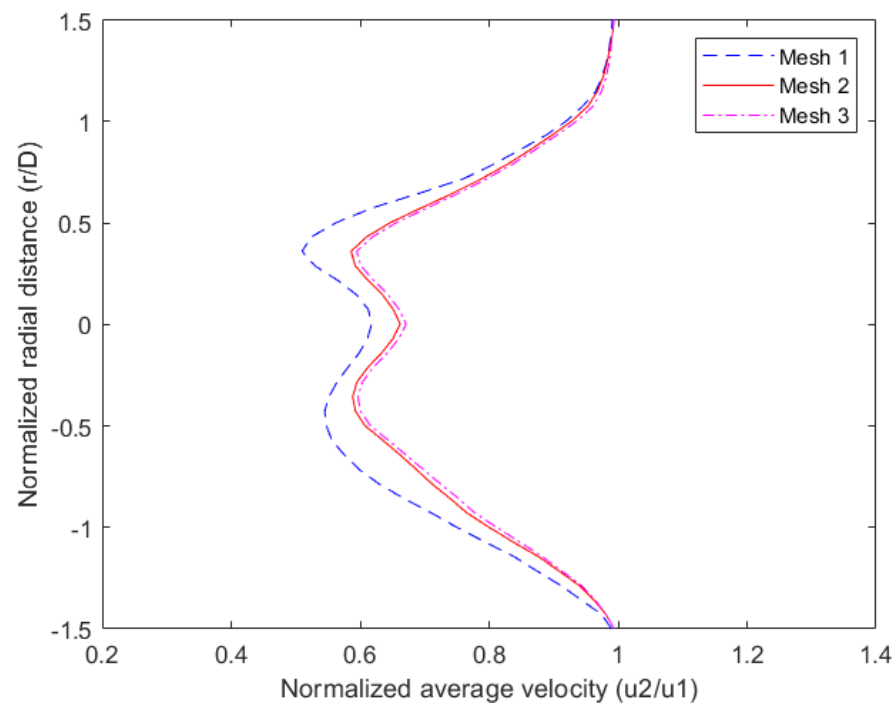
Figure 7. Mesh sensitivity study results of a pentagon platform.

The discretized model of the pentagon configuration of mesh 2 is shown in Figure 8. The pressure-based coupled algorithm is used as the solution method for solving the momentum and continuity equations with second-order upwind discretization for the convection terms of the flow equations. A uniform wind speed of 12.5 m/s is used as a velocity inlet boundary condition with an atmospheric turbulence intensity of 10% and a viscosity ratio of 10%. The atmospheric pressure is selected as the outlet boundary condition. The value of the residual used for obtaining the convergence criteria of the CFD analysis is below 10^{-4}. The velocity contours of the three platform configurations are shown in Figures 9–11. It can be observed that there is a velocity deficit downstream of the wind turbines in all cases which corresponds to the wind turbine wake that is surrounded by the varying turbulence intensity, as shown in Figure 12.
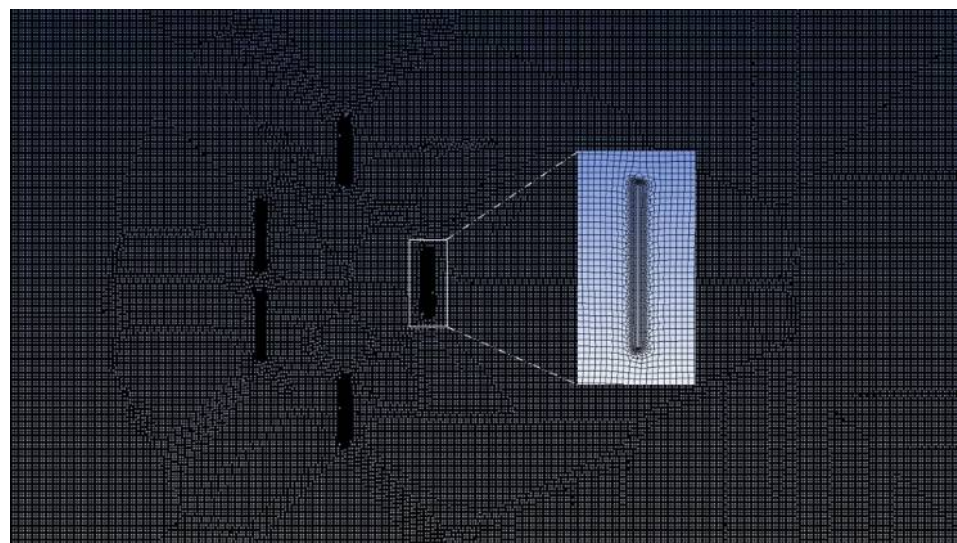

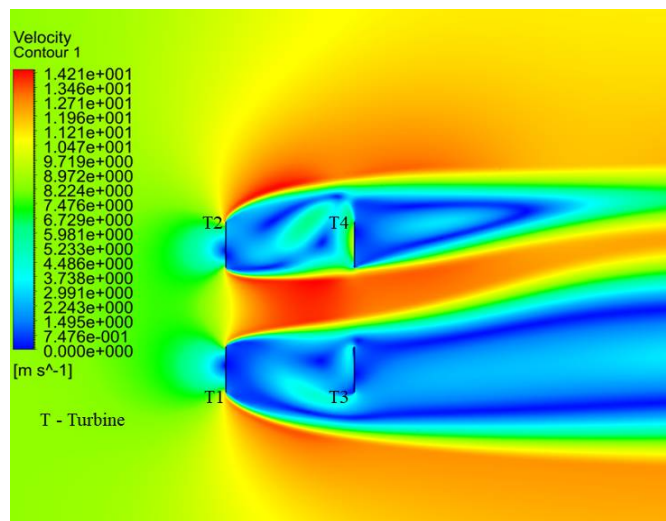**Figure 8.** Discretized model of the pentagon configuration.
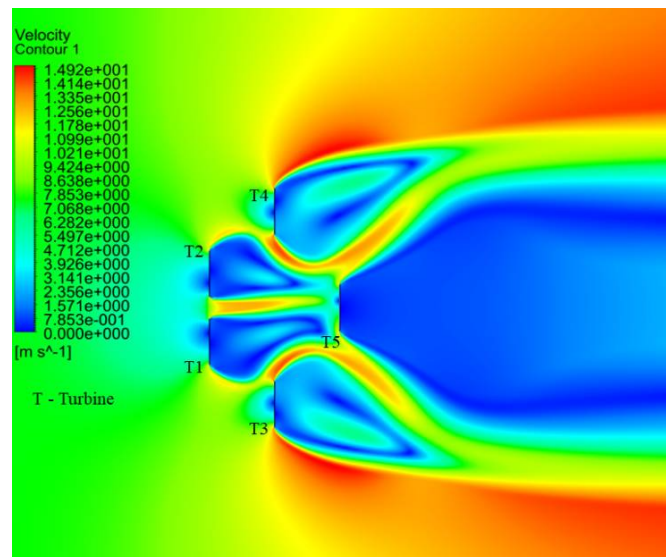
Figure 9. Velocity contours for the square platform.

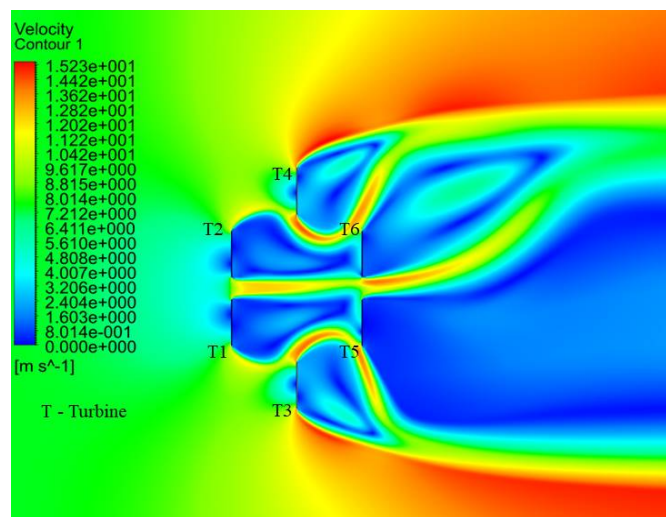**Figure 10.** Velocity contours for the pentagon platform.

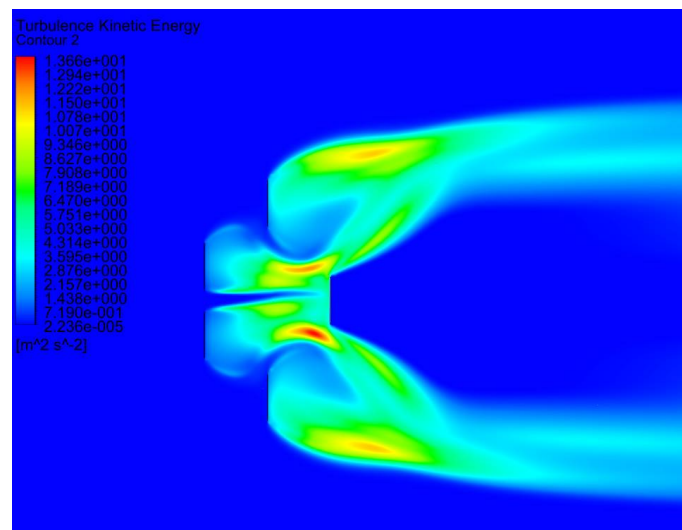**Figure 11.** Velocity contours for the hexagon platform.

Figure 12. Turbulent kinetic energy contours of the pentagon platform.

The normalized velocity profile for the downstream wind turbine at a 2.75 D_r distance downstream for the three platform configurations (T3 for square, T5 for the pentagon and hexagon) is depicted in Figure 13. The velocity profile is approximately similar for the most part in the square and hexagon platforms as the wind turbines are in the direct wake. It can also be observed that the velocity for the pentagon configuration is slightly higher than in the other two cases, which can correlate to the values from the Larsen wake loss model shown in Figure 6.
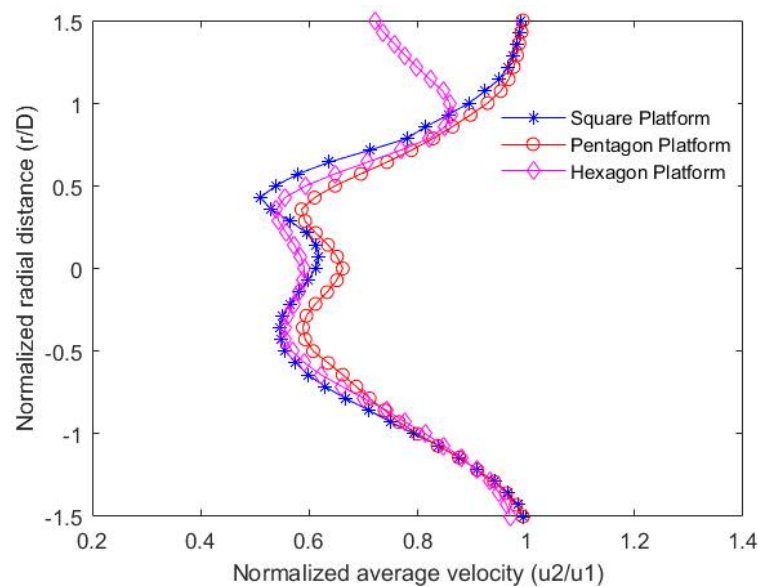
Figure 13. Normalized velocity profile of the downstream turbine.

For the hexagon platform, the top part of the curve shows a reduced velocity due to the presence of the wind turbine (T6) at a 1D rotor diameter. The normalized velocity profile of the analytical Larsen wake model and CFD results at the downstream wind turbine of the pentagon platform is shown in Figure 14. Table 3 shows the comparison between the Larsen wake model and CFD analysis values of normalized streamwise velocity near the downstream wind turbine in the wake for the three platform configurations. The values show a good comparison between the analytical Larsen wake model values and the CFD simulation results.

Figure 14. Comparison of the normalized velocity profile at the downstream turbine.

Table 3. Comparison of normalized streamwise velocity.

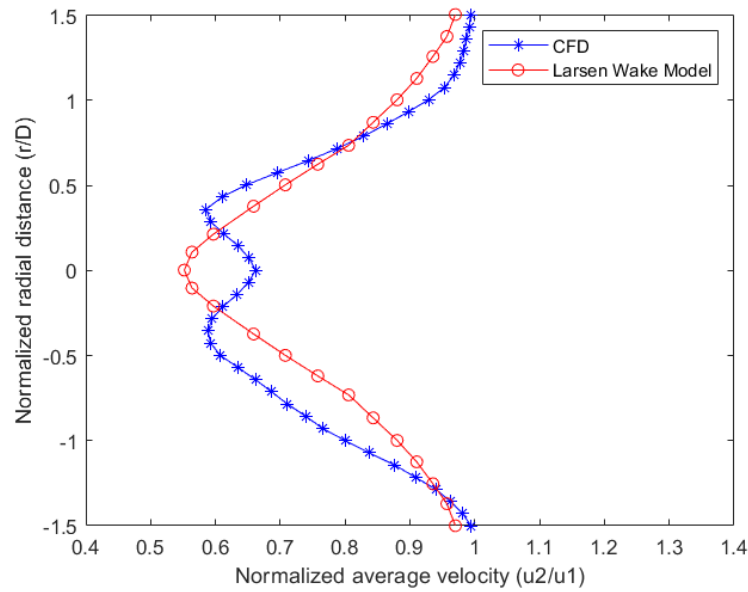|		Larsen Wake Loss Model	CFD
	Maximum	1	0.99
Square	Minimum	0.54	0.51
	Mean	0.77	0.74
	Maximum	1	0.99
Pentagon	Minimum	0.56	0.58
	Mean	0.79	0.77
	Maximum	1	0.97
Hexagon	Minimum	0.54	0.53
	Mean	0.77	0.72

The mean value of normalized streamwise velocity for the wind turbine in the wake in all three cases is approximately equal. However, for the square and hexagon platform configurations, the wake deficit is twice the pentagon platform because of the two wind turbines in direct wake, which means there will be twice the loss in power production. Hence, the pentagon platform configuration is selected for the design of the offshore floating multi-wind turbine platform.

3.2. Platform Configuration

Based on wake effect analyses, the pentagon platform configuration is selected for the design and is modeled in SOLIDWORKS. The main consideration for the platform design is to minimize the wake effects on the downstream wind turbine. The semi-submersible platform for installing the five 8 MW wind turbines on the columns connected by pontoons is shown in Figure 15. The main dimensions considered for this novel platform configuration are provided in Figure 16. To accommodate the 8 MW wind turbine tower base with proper margins, the cylindrical column height and diameter are set to 30 and 15 m, respectively. The diameters of the top and bottom pontoons are 2 and 3.5 m, respectively. The platform is anchored to the seabed by a turret system at the center column with catenary mooring cables attached to the seabed using anchors.
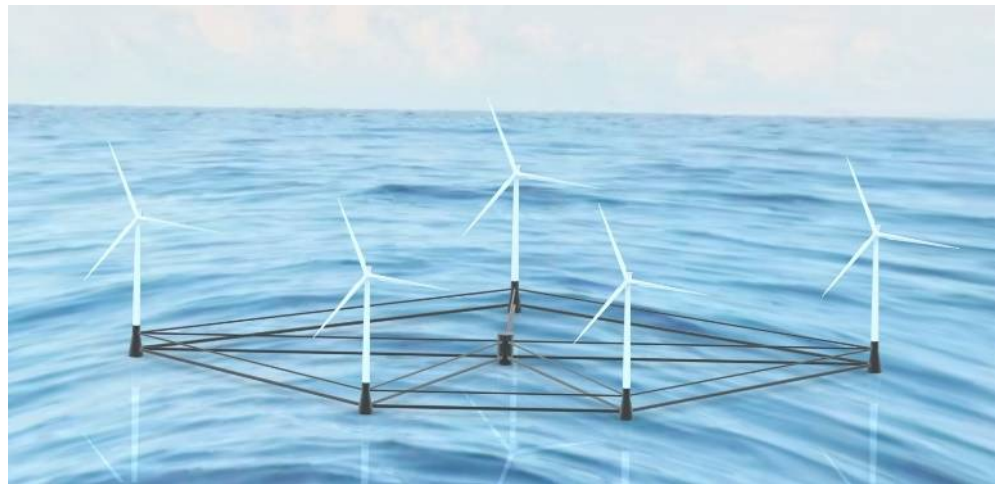
Figure 15. Offshore floating multi-wind turbine platform.
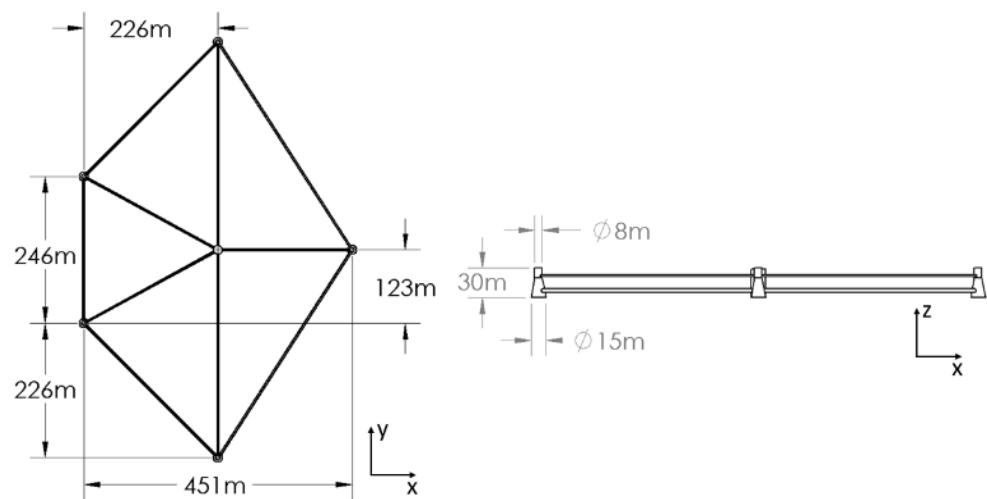
Figure 16. Platform configuration.

The wind turbine used in this study is based on the LEANWIND 8 MW reference wind turbine designed for offshore wind farms [49]. The specifications of the reference wind turbine and designed platform configuration are shown in Tables 4 and 5, respectively.

Table 4. Properties of the wind turbine.

Parameter	Value
Power	8 MW
Rotor diameter	164 m
Hub height	110 m
Nominal rotor speed	10.5 rpm
Cut-in, rated, and cut-out wind speed	4, 12.5, and 25 m/s
Total wind turbine mass	1,038,000 kg

Table 5. Properties of the platform configuration.

Parameter	Value
Water depth	250 m
Platform draft	15 m
Freeboard	15 m
Platform mass	16,081,370 kg
Platform roll inertia	5.027×10^{11} kg.m^2
Platform pitch inertia	3.277×10^{11} kg.m^2
Platform yaw inertia	8.284×10^{11} kg.m^2
Number of mooring lines	4
Mooring line length	600 m

3.3. Hydrostatic Analysis

The hydrostatic performance of the free-floating offshore platform in seawater with a water depth of 250 m is calculated using ANSYS AQWA. The discretized model of the offshore floating platform configuration is shown in Figure 17.
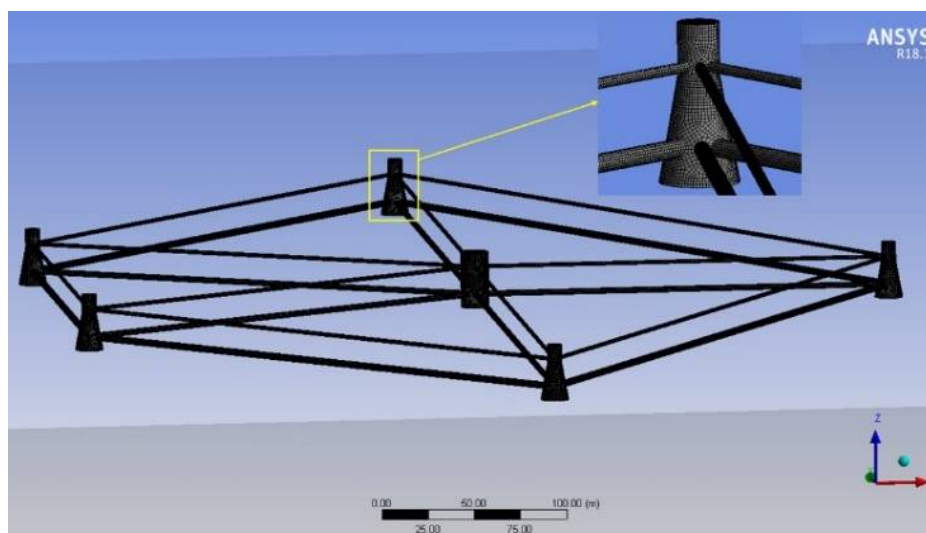

Figure 17. Discretized model of the floating platform.

The hydrostatic stability analysis is used to calculate the ability of the platform to float and keep an upright position in normal environmental conditions. The platform needs to support the overall weight and restrain roll, pitch, and heave motions by providing enough buoyancy [50]. The center of buoyancy, $\vec{X}_B = (X_B, Y_B, Z_B)$, is calculated based on the platform draft of 15 m, as follows [51]:

$$\vec{X}_B = \frac{\rho g \int \vec{X} Z n_3 dS}{F_B} \tag{14}$$

where $\vec{X} = (X, Y, Z)$ is a point on a submerged body, $F_B = \rho g \nabla$ is the buoyancy force, and ∇ is the volumetric displacement of the water. The center of gravity, the center of floatation, and the center of buoyancy calculated from the hydrostatic analysis are shown in Table 6. An active ballast system can be used to balance the location of the center of gravity at the center column. The ballast needed to achieve the desired draft of 15 m is calculated to be 18,930 m^3. The ballast requirement is fulfilled by using the seawater filled in the platform columns.

Table 6. Hydrostatic results of the floating platform.

Parameter	X	Y	Z
Center of gravity above the keel	0 m	0 m	15 m
Center of buoyancy above the keel	0 m	0 m	7 m
Center of flotation above the keel	−5 m	0 m	15 m
Other Properties			
Longitudinal metacentric height	23.5 m		
Transverse metacentric height	23.5 m		
Volumetric displacement	34,620.45 m^3		
Cut waterplane area	534 m^2		
Principal second-moment area	X: 10,433,353 m^4		Y: 1,955,0784 m^4

The semi-submersible platform concept depends on the large waterplane area, draft, and ballast for maintaining stability. The stability requirements for the operating conditions of the wind turbine are mainly focused on the platform roll (rotation about the x-axis), pitch (rotation about the y-axis), and heave (translation in the z-axis) motions. The hydrostatic stiffness values evaluated from the hydrostatic analysis are presented in Table 7. These values of the hydrostatic restoring coefficients show that the platform is stable in all three cases of motion responses. Hydrostatic stiffness is the major contributor to the system stiffness of offshore floating platforms that use slack-type moorings. For the platform to be stable, the stiffness coefficients must oppose small displacements in the platform. The necessary condition in heave, roll, and pitch is that the stiffness values are positive, as provided in Table 7. For heave, this is possible if the waterplane area is not zero, and for roll and pitch, the necessary condition is that the metacentric heights are positive, as shown in Table 7 [52].

Table 7. Hydrostatic stiffness values of the platform.

Variable	Value
Heave (Z)	5.36×10^3 kN/m
Roll (RX)	3.38×10^6 kN.m/°
Pitch (RY)	1.78×10^6 kN.m/°

3.4. Hydrodynamic Analysis

The prediction of the wave-body interaction between the floating platform and the waves is evaluated by performing the hydrodynamic analysis [51,53,54]. The potential flow linear diffraction model is used to calculate the first-order hydrodynamics and wave loadings on the platform in the frequency domain using ANSYS AQWA. The simulation is carried out with encounter frequencies set as 50 for wave directions ranging from 180° to −180°. The added mass, pressures and motions, response amplitude operators (RAOs), and radiation damping are calculated in the hydrodynamic diffraction module. The stability analysis of the platform is carried out using the calculated parameters in the hydrodynamic response module. The structure interpolated pressure contour plot of the platform for a selected frequency of 1.2674 rad/s, incident wave amplitude of 1.5 m, and wave direction angle of 0° is computed as shown in Figure 18.
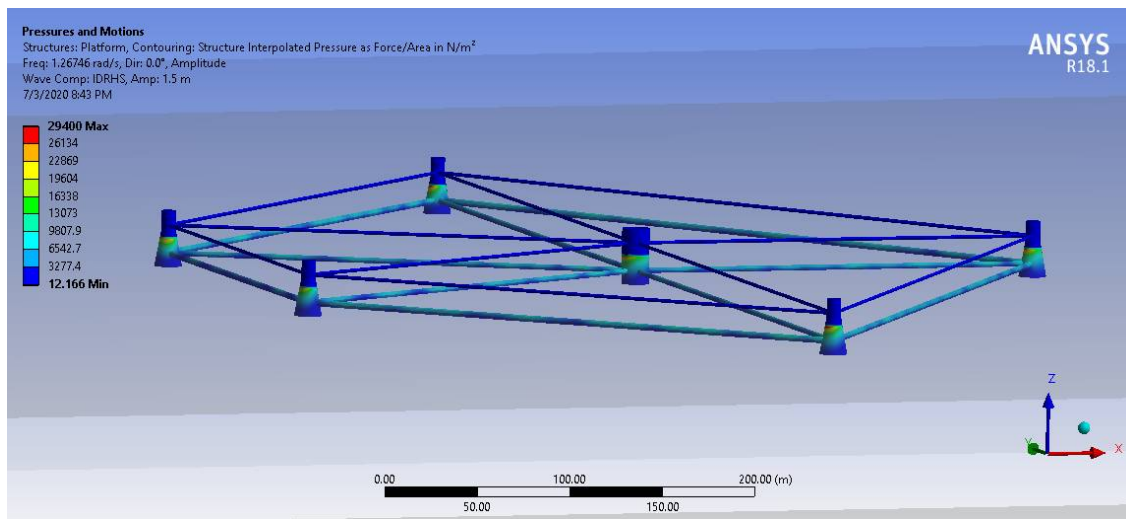
Figure 18. Pressure distribution on the floating platform.

The wave exciting force is calculated using the direct integration of the pressure on the body surface, and the hydrodynamic added mass and damping coefficient is therefore evaluated by the decomposition of the radiation force. The hydrodynamic added mass in the frequency domain for a selected frequency is shown in Table 8.

Table 8. Added mass coefficients of the floating platform.

Variable	Value
Surge	3.2×10^7 kg
Sway	2.3×10^7 kg
Heave	3.6×10^7 kg
Roll	2.2×10^{10} kg.m^2
Pitch	1.1×10^{10} kg.m^2
Yaw	2.6×10^{10} kg.m^2

The natural modes of the platform are found from the stability analysis in the hydrodynamic response module, as shown in Table 9. The natural modes of the platform define the dynamic behavior of the platform.

Table 9. Natural modes of the floating platform.

Mode	Type	Angular Frequency (rad/s)
I	Heave	0.28
II	Pitch	0.34
III	Roll	0.35

The frequency response amplitude operator (RAO) for the heave, pitch, and roll motion of the floating platform is shown in Figures 19–21, respectively.
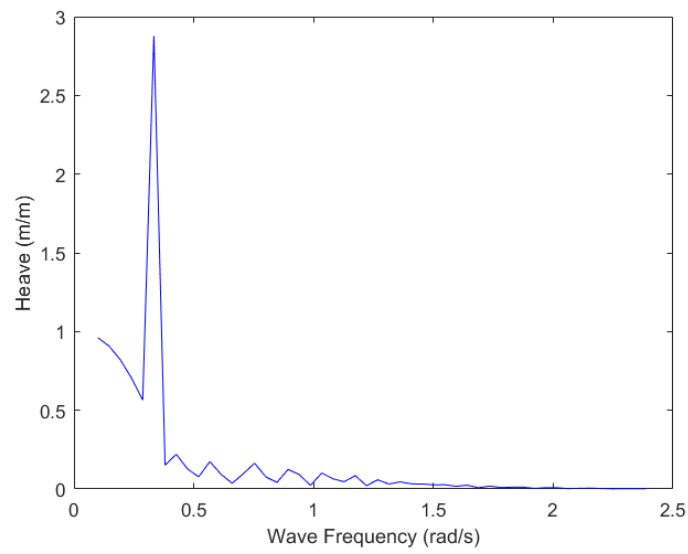
Figure 19. The frequency response of the heave motion of the platform.
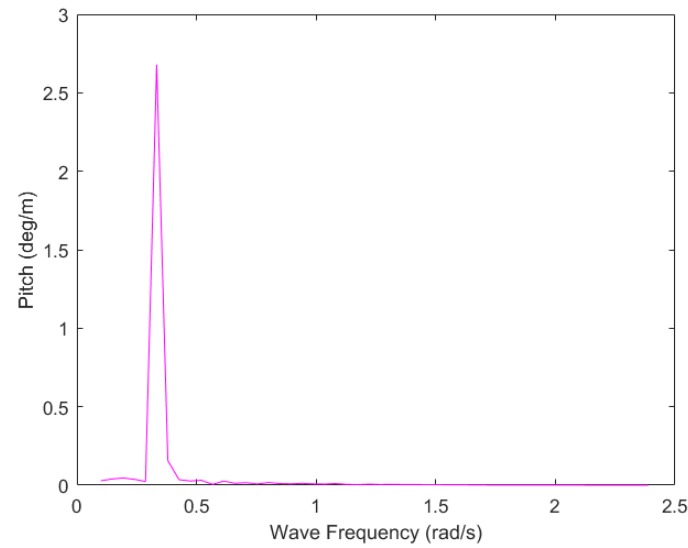
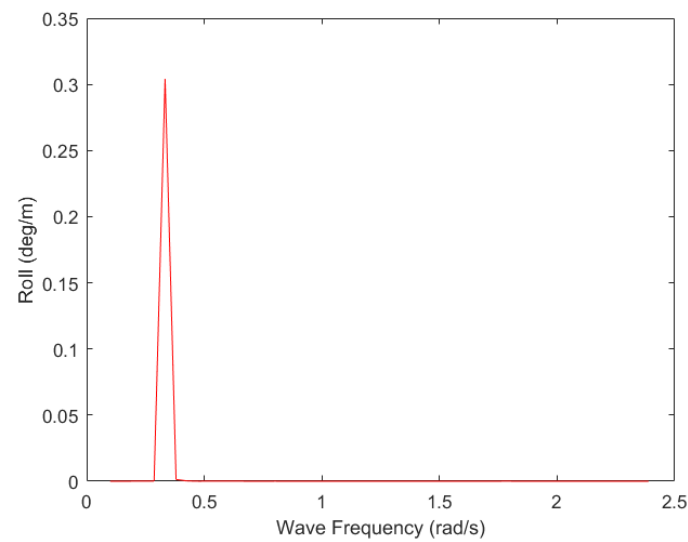**Figure 20.** The frequency response of the pitch motion of the platform.

Figure 21. The frequency response of the roll motion of the platform.

As can be seen in the above figures, the platform responses for the wave heading angle of 0° in all three cases are located below the frequency of 0.5 rad/s. It can also be observed that the frequency response in all three motions peaks around the natural frequency of the platform. The roll response is relatively low because the platform is symmetrical about the x-axis. However, the frequency responses of the pitch and heave motions have relatively higher values, and hence more attention should be paid to pitch and heave motions to ensure a good hydrodynamic performance of the offshore floating platform in coupled wind–wave conditions.

3.5. Cost Analysis

The preliminary cost analysis of the offshore floating multi-wind turbine platform is performed and compared with a conventional single floating wind turbine platform to evaluate the economic feasibility. The main costs considered for this analysis are offshore wind turbine costs (C_T), floating platform cost (C_P), mooring cost (C_M), and installation cost (C_I).

$$Total\ cost\ (TC) = C_T + C_P + C_M + C_I \qquad (15)$$

The cost of an offshore wind turbine is calculated based on the cost per MW (USD/MW) of energy generated (C_{MW}) times the power rating (P_R) of the wind turbine [55–58].

$$C_T = C_{MW} * P_R \qquad (16)$$

The cost of the offshore floating platform is dependent on the cost of material and quantity of the material for the foundation, which can be calculated based on the mass of the platform (M_P) and the cost per ton of steel (C_S).

$$C_P = C_S * M_P \qquad (17)$$

The mooring cost is calculated considering the length of the mooring (L_M), number of mooring lines (N_M), mass per unit length in kg/m (m_l), and the cost per kg of mooring (c_m).

$$C_M = N_M * L_M * m_l * c_m \qquad (18)$$

The installation costs of the system include the installation and transportation costs of the wind turbines, platform, and mooring system.

$$C_I = C_{Install} + C_{transport} \qquad (19)$$

The values of the parameters [59–61] considered for the total cost calculation of the multi-turbine platform are presented in Table 10. Based on the parameter values considered, the total cost per kW (USD/MW) of energy generated for the offshore floating multi-wind turbine platform to install five 8 MW wind turbines is evaluated to be USD1,880,800/MW. For a single wind turbine platform, the total cost per kW (USD/kW) of energy is found to be USD2,025,500/MW, which is significantly higher than the multi-turbine platform. This difference is because of the reduction of mooring and transportation costs in the case of a multi-turbine platform as the five wind turbines use common mooring lines and they are transported with the platform to the installation site after the assembly at the dock. Hence, the proposed multi-wind turbine platform design is a promising concept that can enhance the offshore wind industry.

Table 10. Parameters considered for the analysis.

Variable	Value
P_R	8 MW
C_{MW}	USD1,300,000/MW
M_P	16,081 tons
C_S	USD600/ton
N_M	4
L_M	600 m
m_l	120 kg/m
c_m	USD3/kg
$C_{Install}$	USD290,000/MW
$C_{transport}$	USD140,000/MW

4. Conclusions

The wake interference between the wind turbines can cause a reduction in energy generation, and hence wake analysis is important in the design phase of a multi-wind turbine platform. The wake effect analysis carried out using the Larsen wake model and CFD simulations on three different configurations showed that the pentagon platform configuration is the best possible configuration for installing the multi-wind turbines. The normalized streamwise velocity profile at the downstream wind turbine in wake showed agreement between the analytical Larsen wake model and CFD simulations. The design aspects of the offshore floating multi-wind turbine platform considering the main dimensions of the floater were presented. The hydrostatic analysis showed that the designed platform satisfied the floating stability requirements. The calculated hydrostatic stiffness values proved that the platform was stable in all three motion responses considered. Hydrodynamic stability analysis was carried out to predict the wave-body interaction between the platform and the waves. In all three motion responses evaluated, the peak values occurred around the natural frequency of the platform. The motion responses in frequency responses showed that the pitch and heave motion responses had relatively high values and should be given attention to ensure a good hydrodynamic response of the platform. The cost analysis showed that the proposed multi-turbine platform design is a promising concept that can enhance the offshore wind industry. However, this cost analysis is a preliminary analysis with only the manufacturing and installation costs.

Future work is suggested on the detailed economic analysis to include the design and development costs, operation and maintenance costs, and the cost of electrical subsystems to find the levelized cost of energy. Additionally, further work can be performed by including wind turbines on the platform to analyze the dynamic effects of wind loads and calculate the coupled aero-hydrodynamic responses of the multi-wind turbine platform. Furthermore, the structural analysis of the entire system can be carried out to predict the structural behavior under the coupled wind–wave loading.

Author Contributions: Conceptualization, S.B. and S.O.; methodology, S.B.; software, S.B.; validation, S.B.; formal analysis, S.B.; investigation, S.B.; writing—original draft preparation, S.B.; writing—review and editing, S.B. and S.O.; supervision, S.O. All authors have read and agreed to the published version of the manuscript.

Institutional Review Board Statement: Not applicable.

Informed Consent Statement: Not applicable.

Data Availability Statement: Not applicable.

References

1. Wind Vision. Energy.gov. Available online: https://www.energy.gov/eere/wind/wind-vision (accessed on 27 October 2019).
2. Huijs, F.; de Bruijn, R.; Savenije, F. Concept Design Verification of a Semi-submersible Floating Wind Turbine Using Coupled Simulations. *Energy Procedia* **2014**, *53*, 2–12. [CrossRef]
3. Karimirad, M.; Michailides, C. Dynamic Analysis of a Braceless Semisubmersible Offshore Wind Turbine in Operational Conditions. *Energy Procedia* **2015**, *80*, 21–29. [CrossRef]
4. Karimirad, M.; Michailides, C. V-shaped semisubmersible offshore wind turbine: An alternative concept for offshore wind technology. *Renew. Energy* **2015**, *83*, 126–143. [CrossRef]
5. Liu, Y.; Li, S.; Yi, Q.; Chen, D. Developments in semi-submersible floating foundations supporting wind turbines: A comprehensive review. *Renew. Sustain. Energy Rev.* **2016**, *60*, 433–449. [CrossRef]
6. Mayilvahanan, A.C.; Selvam, P.R. Time Domain Response Analysis of Barge Floater Supporting an Offshore Wind Turbine. *Int. J. Ocean Clim. Syst.* **2011**, *2*, 303–314. [CrossRef]
7. Karimirad, M.; Moan, T. Extreme Dynamic Structural Response Analysis of Catenary Moored Spar Wind Turbine in Harsh Environmental Conditions. *J. Offshore Mech. Arct. Eng.* **2011**, *133*, 041103. [CrossRef]
8. Utsunomiya, T.; Matsukuma, H.; Minoura, S.; Ko, K.; Hamamura, H.; Kobayashi, O.; Sato, I.; Nomoto, Y.; Yasui, K. On Sea Experiment of a Hybrid Spar for Floating Offshore Wind Turbine Using 1/10-Scale Model. *J. Offshore Mech. Arct. Eng.* **2013**, *135*, 529–536. [CrossRef]
9. Dinh, V.N.; Basu, B. On the Modeling of Spar-Type Floating Offshore Wind Turbines. *Key Eng. Mater.* **2013**, *569*, 636–643. [CrossRef]
10. Nihei, Y.; Matsuura, M.; Fujioka, H.; Suzuki, H. An Approach for the Optimum Design of TLP Type Offshore Wind Turbines. In Proceedings of the ASME 2011 30th International Conference on Ocean, Offshore and Arctic Engineering, Rotterdam, The Netherlands, 19–24 June 2011; Volume 5, pp. 219–227. [CrossRef]
11. Jagdale, S.; Ma, Q.W. Practical Simulation On Motions of a TLP-Type Support Structure For Offshore Wind Turbines. In Proceedings of the 20st International Offshore and Polar Engineering Conference, Beijing, China, 20–25 June 2010. Available online: https://www.onepetro.org/conference-paper/ISOPE-I-10-058 (accessed on 4 May 2020).
12. Bae, Y.H.; Kim, M.H. Rotor-floater-mooring coupled dynamic analysis of mono-column-TLP-type FOWT (Floating Offshore Wind Turbine). *Ocean Syst. Eng.* **2011**, *1*, 95–111. [CrossRef]
13. Bashetty, S.; Ozcelik, S. Review on Dynamics of Offshore Floating Wind Turbine Platforms. *Energies* **2021**, *14*, 6026. [CrossRef]
14. Lefranc, M.; Torud, A. Three Wind Turbines on One Floating Unit, Feasibility, Design And Cost. In Proceedings of the Offshore Technology Conference, Houston, TX, USA, 2–5 May 2011. [CrossRef]
15. Hu, C.; Sueyoshi, M.; Liu, C.; Liu, Y. Hydrodynamic Analysis of a Semi-Submersible-Type Floating Wind Turbine. *J. Ocean Wind Energy* **2014**, *1*, 7.
16. Kim, H.C.; Kim, M.H.; Kim, K.H.; Hong, K.; Bae, Y.H. Global Performance of a Square-Type Semi-Submersible KRISO Multi-Unit Floating Wind Turbine; Numerical Simulation vs. Model Test. In Proceedings of the 26th International Ocean and Polar Engineering Conference, Rhodes, Greece, 26 June–1 July 2016; Available online: https://www.onepetro.org/conference-paper/ISOPE-I-16-638 (accessed on 2 May 2020).
17. Kim, K.H.; Hong, J.P.; Park, S.; Lee, K.; Hong, K. An Experimental Study on Dynamic Performance of Large Floating Wave-Offshore Hybrid Power Generation Platform in Extreme Conditions. *J. Korean Soc. Mar. Environ. Energy* **2016**, *19*, 7–17. [CrossRef]
18. Kang, H.; Kim, M.-H.; Kim, K.-H.; Hong, K. Hydroelastic Analysis of Multi-Unit Floating Offshore Wind Turbine Platform (MUFOWT). In Proceedings of the 27th International Ocean and Polar Engineering Conference, San Francisco, CA, USA, 25–30 June 2017. Available online: https://www.onepetro.org/conference-paper/ISOPE-I-17-637 (accessed on 4 May 2020).
19. Lee, H.; Poguluri, S.K.; Bae, Y.H. Performance Analysis of Multiple Wave Energy Converters Placed on a Floating Platform in the Frequency Domain. *Energies* **2018**, *11*, 406. [CrossRef]
20. Jang, H.-K.; Park, S.; Kim, M.-H.; Kim, K.-H.; Hong, K. Effects of heave plates on the global performance of a multi-unit floating offshore wind turbine. *Renew. Energy* **2019**, *134*, 526–537. [CrossRef]
21. Li, S.; Lamei, A.; Hayatdavoodi, M.; Wong, C. Concept Design and Analysis of Wind-Tracing Floating Offshore Wind Turbines. In Proceedings of the ASME 2019 2nd International Offshore Wind Technical Conference, St. Julian's, Malta, 3–6 November 2019. [CrossRef]
22. Lamei, A.; Hayatdavoodi, M.; Wong, C.; Tang, B. On Motion and Hydroelastic Analysis of a Floating Offshore Wind Turbine. In Proceedings of the ASME 2019 38th International Conference on Ocean, Offshore and Arctic Engineering, Scotland, UK, 9–14 June 2019. [CrossRef]
23. Lamei, A.; Hayatdavoodi, M. On motion analysis and elastic response of floating offshore wind turbines. *J. Ocean Eng. Mar. Energy* **2020**, *6*, 71–90. [CrossRef]
24. Kim, H.C.; Jang, H.K.; Kim, M.H.; Bee, Y.H. Coupled Dynamic Analysis of a MUFOWT with Transient Broken-blade Incident. In Proceedings of the 25th International Ocean and Polar Engineering Conference, Kona, HI, USA, 21–26 June 2015. Available online: https://www.onepetro.org/conference-paper/ISOPE-I-15-617 (accessed on 23 June 2020).
25. Bae, Y.H.; Kim, M.-H. The Dynamic Coupling Effects of a MUFOWT (Multiple Unit Floating Offshore Wind Turbine) with Partially Broken Blade. *J. Ocean Wind Energy* **2015**, *2*. [CrossRef]

26. González-Longatt, F.; Wall, P.; Terzija, V. Wake effect in wind farm performance: Steady-state and dynamic behavior. *Renew. Energy* **2012**, *39*, 329–338. [CrossRef]

27. Adaramola, M.S.; Krogstad, P.-Å. Experimental investigation of wake effects on wind turbine performance. *Renew. Energy* **2011**, *36*, 2078–2086. [CrossRef]

28. Kim, K.; Kim, H.; Lee, J.; Kim, S.; Paek, I. Design and performance analysis of control algorithm for a floating wind turbine on a large semi-submersible platform. *J. Phys. Conf. Ser.* **2016**, *753*, 092017. [CrossRef]

29. Bashetty, S.; Ozcelik, S. Design and Stability Analysis of an Offshore Floating Multi-Turbine Platform. In *2020 IEEE Green Technologies Conference (GreenTech)*; IEEE: New York, NY, USA, 2020; pp. 184–189. [CrossRef]

30. Larsen, G.C. *A Simple Wake Calculation Procedure*; Risø National Laboratory: Roskilde, Denmark, 1988. Available online: https://orbit.dtu.dk/en/publications/a-simple-wake-calculation-procedure (accessed on 3 May 2020).

31. Pierik, J.T.G.; Dekker, J.W.M.; Braam, H.; Bulder, B.H.; Winkelaar, D.; Larsen, G.C.; Morfiadakis, E.; Chaviaropoulos, P.; Derrick, A.; Molly, J.P. European wind turbine standards II (EWTS-II). In *Wind Energy for the Next Millennium. Proceedings*; James and James Science Publishers: London, UK, 1999; pp. 568–571. Available online: https://orbit.dtu.dk/en/publications/european-wind-turbine-standards-ii-ewts-ii (accessed on 4 May 2020).

32. Schepers, J.G. ENDOW. Validation and Improvement of ECN's Wake Model (Technical Report) | ETDEWEB. Available online: https://www.osti.gov/etdeweb/biblio/20360050 (accessed on 24 June 2020).

33. Larsen, G.C. *A simple Stationary Semi-Analytical Wake Model*; Risø National Laboratory for Sustainable Energy, Technical University of Denmark: Lyngby, Denmark, 2009. Available online: https://orbit.dtu.dk/en/publications/a-simple-stationary-semi-analytical-wake-model (accessed on 4 May 2020).

34. Frandsen, S. *Turbulence and Turbulence-Generated Structural Loading in Wind Turbine Clusters (Thesis/Dissertation) | ETDEWEB*; Risø National Laboratory: Roskilde, Denmark, 2007. Available online: https://backend.orbit.dtu.dk/ws/portalfiles/portal/12674798/ris_r_1188.pdf (accessed on 4 May 2020).

35. Frohboese, P.; Hassan, G. Thrust coefficients used for estimation of wake effects for fatigue load calculation. In Proceedings of the European Wind Energy Conference & Exhibition 2010, Warsaw, Poland, 20–23 April 2010; p. 10. Available online: http://proceedings.ewea.org/ewec2010/allfiles2/207_EWEC2010presentation.pdf (accessed on 12 December 2020).

36. Arany, L.; Bhattacharya, S.; Macdonald, J.; Hogan, S.J. Design of monopiles for offshore wind turbines in 10 steps. *Soil Dyn. Earthq. Eng.* **2017**, *92*, 126–152. [CrossRef]

37. Wu, Y.-T.; Porté-Agel, F. Atmospheric Turbulence Effects on Wind-Turbine Wakes: An LES Study. *Energies* **2012**, *5*, 5340–5362. [CrossRef]

38. Barthelmie, R.; Hansen, O.F.; Enevoldsen, K.; Højstrup, J.; Frandsen, S.; Pryor, S.; Larsen, S.; Motta, M.; Sanderhoff, P. Ten Years of Meteorological Measurements for Offshore Wind Farms. *J. Sol. Energy Eng.* **2005**, *127*, 170–176. [CrossRef]

39. Argyle, P.; Watson, S.; Montavon, C.; Jones, I.; Smith, M. Modelling turbulence intensity within a large offshore wind farm. *Wind Energy* **2018**, *21*, 1329–1343. [CrossRef]

40. Archer, C.L.; Vasel-Be-Hagh, A.; Yan, C.; Wu, S.; Pan, Y.; Brodie, J.F.; Maguire, A.E. Review and evaluation of wake loss models for wind energy applications. *Appl. Energy* **2018**, *226*, 1187–1207. [CrossRef]

41. Menter, F.R. Two-equation eddy-viscosity turbulence models for engineering applications. *AIAA J.* **1994**, *32*, 1598–1605. [CrossRef]

42. Versteeg, H.K.; Malalasekera, W. *An Introduction to Computational Fluid Dynamics: The Finite Volume Method*, 2nd ed.; Pearson Education Ltd.: Harlow, UK; New York, NY, USA, 2007.

43. Menter, F.R. Review of the shear-stress transport turbulence model experience from an industrial perspective. *Int. J. Comput. Fluid Dyn.* **2009**, *23*, 305–316. [CrossRef]

44. Keck, R.-E. A numerical investigation of nacelle anemometry for a HAWT using actuator disc and line models in CFX. *Renew. Energy* **2012**, *48*, 72–84. [CrossRef]

45. Shakoor, R.; Hassan, M.Y.; Raheem, A.; Wu, Y.-K. Wake effect modeling: A review of wind farm layout optimization using Jensen's model. *Renew. Sustain. Energy Rev.* **2016**, *58*, 1048–1059. [CrossRef]

46. Bartl, J.; Pierella, F.; Sætrana, L. Wake Measurements Behind an Array of Two Model Wind Turbines. *Energy Procedia* **2012**, *24*, 305–312. [CrossRef]

47. Langtry, R.; Gola, J.; Menter, F. Predicting 2D Airfoil and 3D Wind Turbine Rotor Performance using a Transition Model for General CFD Codes. In *44th AIAA Aerospace Sciences Meeting and Exhibit*; American Institute of Aeronautics and Astronautics: Reston, VA, USA, 2006. [CrossRef]

48. Lanzafame, R.; Mauro, S.; Messina, M. 2D CFD Modeling of H-Darrieus Wind Turbines Using a Transition Turbulence Model. *Energy Procedia* **2014**, *45*, 131–140. [CrossRef]

49. Desmond, C.; Murphy, J.; Blonk, L.; Haans, W. Description of an 8 MW reference wind turbine. *J. Phys. Conf. Ser.* **2016**, *753*, 092013. [CrossRef]

50. Butterfield, S. Engineering Challenges for Floating Offshore Wind Turbines. In *Proceedings of the 2005 Copenhagen Offshore Wind Conference*; Copenhagen, Denmark, 26–28 October 2005, p. 13. Available online: https://www.nrel.gov/docs/fy07osti/38776.pdf (accessed on 5 July 2022).

51. Newman, J.N. Marine Hydrodynamics, 40th Anniversary Edition | The MIT Press. Available online: https://mitpress.mit.edu/books/marine-hydrodynamics-40th-anniversary-edition (accessed on 3 May 2020).

52. Bayati, I.; Jonkman, J.; Robertson, A.; Platt, A. The effects of second-order hydrodynamics on a semisubmersible floating offshore wind turbine. *J. Phys. Conf. Ser.* **2014**, *524*, 012094. [CrossRef]

53. Veritas, D.N. *DNV-OS-J101: Design of Offshore Wind Turbine Structures*; DNV: Copenhagen, Denmark, 2014.

54. DNV GL Launches Revised Design & Certification Standards for Floating Wind Turbines. Windpower Engineering & Development. Available online: https://www.windpowerengineering.com/dnv-gl-launches-revised-design-certification-standards-for-floating-wind-turbines/ (accessed on 26 October 2019).

55. Jonkman, J.; Matha, D. *Quantitative Comparison of the Responses of Three Floating Platforms*; NREL/CP-500-46726; National Renewable Energy Lab.: Golden, CO, USA, 2010. Available online: https://www.osti.gov/biblio/974453 (accessed on 28 June 2020).

56. Beiter, P.; Musial, W.; Kilcher, L.; Maness, M.; Smith, A. *An Assessment of the Economic Potential of Offshore Wind in the United States from 2015 to 2030*; NREL/TP–6A20-67675, 1349721; National Renewable Energy Lab.: Golden, CO, USA, 2017. Available online: http://www.osti.gov/servlets/purl/1349721/ (accessed on 20 May 2019).

57. Kausche, M.; Adam, F.; Dahlhaus, F.; Großmann, J. Floating offshore wind—Economic and ecological challenges of a TLP solution. *Renew. Energy* **2018**, *126*, 270–280. [CrossRef]

58. Castro-Santos, L.; Filgueira-Vizoso, A.; Carral-Couce, L.; Formoso, J.Á.F. Economic feasibility of floating offshore wind farms. *Energy* **2016**, *112*, 868–882. [CrossRef]

59. Musial, W.D.; Beiter, P.C.; Nunemaker, J. *Cost of Floating Offshore Wind Energy Using New England Aqua Ventus Concrete Semisubmersible Technology*; NREL/TP-5000-75618; National Renewable Energy Lab.: Golden, CO, USA, 2020. [CrossRef]

60. Zountouridou, E.I.; Kiokes, G.C.; Chakalis, S.; Georgilakis, P.S.; Hatziargyriou, N.D. Offshore floating wind parks in the deep waters of Mediterranean Sea. *Renew. Sustain. Energy Rev.* **2015**, *51*, 433–448. [CrossRef]

61. Myhr, A.; Bjerkseter, C.; Ågotnes, A.; Nygaard, T.A. Levelised cost of energy for offshore floating wind turbines in a life cycle perspective. *Renew. Energy* **2014**, *66*, 714–728. [CrossRef]